Biomimetic inorganic-organic hybrid nanoparticles from magnesium-substituted amorphous calcium phosphate clusters and polyacrylic acid molecules

Na Li [a,b,1], Wei Cui [a,b,1], Peifang Cong [c], Jie Tang [e], Yong Guan [d], Caihao Huang [a,b], Yunen Liu [c], Chengzhong Yu [e], Rui Yang [a,b], Xing Zhang [a,b,*]

[a] *Institute of Metal Research, Chinese Academy of Sciences, Shenyang, Liaoning, 110016, China*
[b] *School of Materials Science and Engineering, University of Science and Technology of China, Hefei, Anhui, 230026, China*
[c] *Department of Emergency Medicine, General Hospital of Northern Theater Command, Shenyang, Liaoning, 110016, China*
[d] *National Synchrotron Radiation Laboratory, University of Science and Technology of China, Hefei, Anhui, 230029, China*
[e] *Australian Institute for Bioengineering and Nanotechnology, The University of Queensland, Brisbane, QLD, 4072, Australia*

ARTICLE INFO

ABSTRACT

Amorphous calcium phosphate (ACP) has been widely found during bone and tooth biomineralization, but the meta-stability and labile nature limit further biomedical applications. The present study found that the chelation of polyacrylic acid (PAA) molecules with Ca^{2+} ions in Mg-ACP clusters ($\sim$2.1 $\pm$ 0.5 nm) using a biomineralization strategy produced inorganic-organic Mg-ACP/PAA hybrid nanoparticles with better thermal stability. Mg-ACP/PAA hybrid nanoparticles ($\sim$24.0 $\pm$ 4.8 nm) were pH-responsive and could be efficiently digested under weak acidic conditions (pH 5.0–5.5). The internalization of assembled Mg-ACP/PAA nanoparticles by MC3T3-E1 cells occurred through endocytosis, indicated by laser scanning confocal microscopy and cryo-soft X-ray tomography. Our results showed that cellular lipid membranes remained intact without pore formation after Mg-ACP/PAA particle penetration. The assembled Mg-ACP/PAA particles could be digested in cell lysosomes within 24 h under weak acidic conditions, thereby indicating the potential to efficiently deliver encapsulated functional molecules. Both the *in vitro* and *in vivo* results preliminarily demonstrated good biosafety of the inorganic-organic Mg-ACP/PAA hybrid nanoparticles, which may have potential for biomedical applications.

1. Introduction

Amorphous calcium phosphate (ACP) plays an important role in the biomineralization of bone, teeth, and other tissues, serving as a precursor for apatite minerals [1–5]. Previous studies revealed that ACP was found intracellularly in mineralizing cells, especially as mineral granules in mitochondria [6,7], which can be transported in matrix vesicles via lysosomes and secreted by exocytosis to the extracellular matrix for biomineralization [8]. The C-terminal end of collagen molecules with a positive net charge promoted the infiltration of these ACP granules to collagen fibrils [9]. The ACP granules further transform into bone apatite crystals along the long-axis of collagen via a step-flow cluster/dissolution growth mechanism [10,11]. Additionally, ACP

nanoparticles were found in teeth [12] and shown to transport soluble macromolecules, such as bacterial peptidoglycan and orally fed protein antigens, from the small intestine lumen to immune cells [3]. Although ACP has good biocompatibility and versatile functions *in vivo*, its meta-stability and labile nature limit further biomedical applications [13].

A recent study reported that ACP nucleation occurred through the aggregation of prenucleation clusters ($\sim$0.7–1.1 nm) in a biomimetic precipitation process [14]. Acidic non-collagenous proteins (NCPs), such as osteonectin, osteopontin, osteocalcin, and phosphophoryn, stabilized ACP clusters and aggregates by forming complex phases, which may more easily infiltrate collagen fibrils [15–19]. Furthermore, organic molecules, such as polyacrylic acid (PAA), polyaspartic acid (PASP), and

trimethylamine (TEA), have been used instead of NCPs to improve the stability of ACP during biomineralization [20,21]. In addition to organic molecules, magnesium (Mg^{2+}) ions are commonly found in biogenic ACP (hereinafter referred to as Mg-ACP), such as human dental enamel, and have been shown to stabilize Mg-ACP by inhibiting further crystallization because of the higher hydration energy of Mg^{2+} ions (~303.9 kcal/mol) relative to Ca^{2+} ions (~182.0 kcal/mol) [22,23]. Organic additives and Mg^{2+} ions have also been reported to improve the stability of amorphous calcium carbonate (ACC) during biomineralization and/or chemical synthesis [24–26]. For example, PAA molecules with abundant carboxylic acid functional groups show the ability to improve the stability of ACC due to the intercalation between the carboxylate and Ca^{2+} ions that can inhibit further crystallization of ACC [24]. Poly-ethylene glycol (PEG) decorated on the surface of ACC also decrease the degradation and extend the blood circulation time of Fe-ACC nano-particles [25]. These inorganic-organic hybrid nanoparticles show advantageous functions for drug delivery [25,27,28]. Although organic molecules and Mg^{2+} ions were found to inhibit ACP crystallization, respectively [20–23], the synergistic effects of Mg^{2+} ions and PAA molecules on the biomimetic stabilization of ACP clusters have not yet been reported. Moreover, cellular interactions and biosafety of ACP hybrid nanoparticles remain poorly understood.

In the present study, Mg-ACP and PAA (hereinafter referred to as Mg-ACP/PAA) hybrid nanoparticles were synthesized using a biomineralization strategy. The chelation of PAA molecules in synergy with Mg^{2+} substitution retained Mg-ACP clusters (~2.1 ± 0.5 nm) and significantly improved thermal stability of the Mg-ACP/PAA nanoparticles. Interactions between the assembled Mg-ACP/PAA nanoparticles and MC3T3-E1 cells under live-cell conditions were studied using a real-time cell-based assay (RTCA) technique. The internalization and degradation of these nanoparticles by MC3T3-E1 cells and delivery of functional molecules (e.g., fluorescent molecules) *in vitro* were investigated using cryo-soft X-ray tomography (Cryo-SXT), laser scanning confocal microscopy (LSCM), and flow cytometry (fluorescence-activated cell sorting [FACS]) analyses. Biosafety of the Mg-ACP/PAA nanoparticles was evaluated using both *in vitro* and *in vivo* models.

2. Materials and methods

2.1. Chemical synthesis of nanoparticles

The Mg-ACP/PAA nanoparticles were produced by wet chemical precipitation. Powders of Mg(NO$_3$)$_2$·6H$_2$O (0.038 g, final concentration of 3 mmol/L) and Ca(NO$_3$)$_2$·4H$_2$O (0.319 g, final concentration of 27 mmol/L) were dissolved in 50 ml of ultrapure water to obtain homogeneous solution A with a Ca/Mg molar ratio of 9. Powders of (NH$_4$)$_2$HPO$_4$ (0.132 g, final concentration of 5 mmol/L) and PAA (40 mg, final concentration of 0.1 mmol/L; Aladdin Bio-Chem Technology Co., Ltd., Shanghai, China) were dissolved in 200 ml of ultrapure water. The pH was adjusted to 9 by 25–28 wt% ammonium hydroxide solution to obtain solution B. Solution A was slowly added to solution B in a dropwise fashion at a speed of 2 ml/min. The above solution mixture was stirred at 300 rotations per minute (rpm) for 1 h. Precipitates were collected by centrifugation at 4000 rpm for 5 min. The precipitates were further dialyzed with deionized water in an 8000–14000 Da dialysis tube for 24 h to remove excess PAA molecules and reactants. The Mg-ACP/PAA samples were finally obtained by freeze drying for 12 h (Gold SIM International Group, Miami, U.S.A.). For the synthesis of fluorescein isothiocyante (FITC)-incorporated Mg-ACP/PAA (Mg-ACP/PAA/FITC) samples, 10 mg FITC (Mao Kang, Biotechnology Co. Ltd., Shanghai, China) powders were dissolved in 50 ml of solution A together with Ca(NO$_3$)$_2$·4H$_2$O and Mg(NO$_3$)$_2$·6H$_2$O powders. The other steps were the same as described above.

For the synthesis of ACP samples, 100 ml of 0.45 mol/L Ca(NO$_3$)$_2$ solution was added to 100 ml of 0.3 mol/L (NH$_4$)$_2$HPO$_4$ (pH 10.0, adjusted by 25–28 wt% ammonium hydroxide solution). The above solution mixture was stirred at 300 rpm for 1 h. Precipitates were collected by centrifugation at 4000 rpm for 5 min. The ACP and Mg-ACP samples were finally obtained by freeze drying for 12 h. For the synthesis of Mg-ACP samples, 0.05 mol/L Mg(NO$_3$)$_2$ was mixed in 100 ml of 0.45 mol/L Ca(NO$_3$)$_2$ solution before adding it to 100 ml of 0.3 mol/L (NH$_4$)$_2$HPO$_4$ (pH 9.0, adjusted by 25–28 wt% ammonium hydroxide solution). All of the other steps were the same as above for the synthesis of ACP samples. HA and Mg-TCP nanoparticles were obtained by aging the above ACP and Mg-ACP, respectively, in a water bath at 80 °C for 6 h before centrifugation. All of the chemicals were obtained from Sino-pharm Chemical Reagent Co., Ltd. (Beijing, China) unless otherwise specified.

2.2. In vitro dissolution experiment

Phosphate buffer solutions (pH 5.0, 5.5, and 6.0) were prepared by mixing 0.1 mol/L Na$_2$HPO$_4$ and 0.1 mol/L NaH$_2$PO$_4$ solutions. Mg-ACP/PAA, TCP, and HA samples were dissolved into phosphate buffer solutions (pH 5.0 and 5.5) to simulate degradation in lysosomes. Mg-ACP/PAA nanoparticles were dissolved in phosphate buffer solutions (pH 5.0 and 6.0) for 10 min, 1 h, 4 h, and 6 h to simulate degradation in lysosomes and early endosomes. The Ca^{2+} contents that were dissolved in the phosphate buffer solutions were measured using inductively coupled plasma mass spectrometry (ICP-MS; Prodigy, Leeman Labs, Hudson, U.S.A.) with three replicates for each sample.

2.3. Material composition and morphology analysis

The mineral phases were identified using an X-ray diffractometer (Rigaku D/max 2400 diffractometer, Tokyo, Japan) that was operated at 40 kV with a Cu Kα1 of 1.5418 Å. The 2θ range of 20–70° with a step size of 0.04° was used. Chemical bonding information for the powder samples was analyzed using a Fourier-transform infrared spectrometer (Tensor 27, Bruker, Billerica, U.S.A.). The attenuated total reflection (ATR) mode with a wavenumber in the range of 600–3600 cm^{-1} and step size of 2 cm^{-1} was used. Mg-ACP/PAA hybrid nanoparticles were dissolved in 2 wt% hydrochloric solution to measure the Ca and Mg content (20 mg/L nanoparticle solutions), and PO$_4^{3-}$ content (100 mg/L nanoparticle solutions) by ICP-MS with three replicates for each sample.

The morphology and crystalline information of the samples were analyzed using a Tecnai F30 transmission electron microscope (FEI, Hillsboro, U.S.A.) at an accelerating voltage of 300 kV. The powder samples were ultrasonically dispersed in ethanol at 100 Hz for 5 min. The suspension was dropped onto a copper grid with holey carbon film (Beijing Zhongjingkeyi Technology Co., Ltd., Beijing, China) for transmission electron microscopy (TEM) observation. The size distribution of the nanoparticles was tested using a Zetasizer Nano ZSP laser particle analyzer (Malvern, Malvern, U.K.).

The thermodynamic properties (TGA/DSC) of the Mg-ACP/PAA sample were analyzed using a thermal analyzer (Netzsch STA 449F3, Selb, Germany). The surface areas of the Mg-ACP/PAA, Mg-TCP, and HA powders were measured using the Brunauer, Emmett, and Teller (BET) method (Micromeritics ASAP 2020, Norcross, U.S.A.) after degassing under vacuum at 150 °C. Elastic moduli of the nanoparticles were evaluated using Peak Force Quantitative Nanomechanical Mapping (PeakForce QNM) mode by a Dimension Icon atomic force microscope (Bruker, Newark, U.S.A.). The experimental details were described in the supplementary material.

2.4. Cell culture and nanoparticle treatment

MC3T3-E1 cells were purchased from the cell bank of the Chinese Academy of Sciences (Shanghai, China), which were cultured with normal culture medium (α-minimal essential medium [MEM]) supplemented with 10% fetal bovine serum (Thermo Scientific HyClone, Logan, U.S.A.) and 1% antibiotic/antimycotic (Invitrogen, Carlsbad, U.

S.A.) at 37 °C in a humidified atmosphere with 5% CO_2. For nanoparticle treatment, the Mg-ACP/PAA nanoparticles were dispersed in serum-free α-MEM (17–272 μg/ml), which were used for MC3T3-E1 cell culture to allow the internalization of nanoparticles for 1–4 h and then replaced with normal culture medium.

Cell viability was determined using the live/dead viability assay. MC3T3-E1 cells were cultured in a 96-well culture plate with 1×10^4 cells/well for 24 h MC3T3-E1 cells were then cultured with Mg-ACP/PAA nanoparticle medium (136 μg/ml) and serum-free α-MEM (control group) to allow the internalization of nanoparticles for 4 h, which were further cultured with normal culture medium for 24 h MC3T3-E1 cells were incubated with dual-color dyes (2 μM propidium iodide (PI) and 1 μM Calcein AM, Sigma-Aldrich, St. Louis, MO, U.S.A.) at 37 °C for 15 min according to the manufacturer's protocol. Fluorescence imaging was conducted using a Leica SP2 laser scanning confocal microscope (Leica, Solms, Germany). The area of Calcein-stained cells was measured and divided by the total area of counted cells to determine the percentage of viability using ImageJ software. The average value of viability from three images was used for each sample.

Holographic imaging of cell culture in parallel was performed using a lens-free video device with a resolution of 1–2 μm (IPRASENSE Cytonote, Montpellier, France). Fluorescence imaging with Lyso-Tracker red staining was performed using a Leica TCS SP2 confocal microscope (350–460 nm laser line). The detection of intracellular Ca^{2+} ions was performed by FACS (FACSCalibur Cell Sorting System, BD Biosciences, San Jose, U.S.A.) at a 525 nm emission wavelength. The experimental details were described in the supplementary material.

2.5. Dynamic monitoring of cytotoxic response using the RTCA cell impedance system

The effects of Mg-ACP/PAA nanoparticles on cell viability were studied using an xCELLigence DP real-time cell analyzer (Roche, Basel, Switzerland). Sixteen-well plates with gold electrodes at the bottom were used to culture MC3T3-E1 cells, from which the electrical impedance during cell growth was measured in real time. Electrical impedance is translated as the Cell Index (CI; a dimensionless parameter). The following Equation (1) was used to calculate the CI:

$$CI = \max_{i=1 \to N}\left(\frac{R_{cell}(f_i)}{R_b(f_i)} - 1\right) \qquad (1)$$

where $R_b(f)$ and $R_{cell}(f)$ are the unimpeded electrical impedance and electrical impedance of cell adhesion, respectively, and N is the number of frequency points where the electrical impedance was detected. When cells are not present or adhered on the electrodes, the CI is zero. As the number of cells that adhere on electrodes increases, the CI increases. The CI variations are displayed in a real-time plot by RTCA 2.0 software. The normalized CI was indicative of the level of cell adhesion and thus associated with cell viability [29,30].

MC3T3-E1 cells at 2500 cells/well were cultured with normal culture medium (100 μl per well) for 25 h, and the CI was normalized to 1.0. The culture medium was removed and replaced with 100 μl of nanoparticle medium (17, 34, 68, 136, and 272 μg/ml) in serum-free α-MEM, and α-MEM without serum was used for the control group for 4 h. These cells were further cultured with normal medium for 36 h. The impedance was monitored at 15 min intervals using RTCA 2.0 software.

2.6. Cryo-soft X-ray tomography imaging

The Cryo-SXT experiments were performed using an X-ray microscope at beamline BL07W at the National Synchrotron Radiation Laboratory (Hefei, China). One-hundred-mesh nickel grids (Zhongjingkeyi Technology Co., Ltd., Beijing, China) were used to culture MC3T3-E1 cells. Cells on the nickel grids were placed in a freezer plunge and rapidly transferred to a cryopreserving container to freeze the cells

inside liquid nitrogen to retain cellular structures. The specimens were then transferred to the soft X-ray imaging vacuum cryogenic chamber through the side-entry holder for further imaging. In this experiment, the X-rays were focused by an elliptical capillary condenser. The soft X-ray energies ranged from 280 to 700 eV, with a spatial resolution of 30 nm. The whole system can perform absorption imaging coupled with a microzone plate [31].

2.7. In vivo biosafety test

Twenty-four male Sprague-Dawley rats (180–200 g) were supplied by the Liaoning Changsheng biotechnology Co., Ltd. (Benxi, Liaoning, China). The rats were fed a standard diet and given free access to water in a room maintained at 20 °C ± 2 °C with 55–65% humidity. The rats were randomly divided into three groups with 6 rats/group. Each rat in the two experimental groups was injected with 0.5 ml of Mg-ACP/PAA nanoparticles in saline (136 μg/ml) via the tail vein. Rats in the control group were injected with an equal volume of normal saline. Blood samples were immediately collected after the saline injection for the control group and 24 and 72 h after the injection of the Mg-ACP/PAA nanoparticle solutions in the two experimental groups. Routine blood biochemistry was evaluated. Anticoagulated whole-blood samples were analyzed using a Coulter LH 780 Analyzer (LH SlideMaker, Beckman Coulter, Brea, U.S.A.). The indexes consisted of the white blood cell (WBC) count, neutrophil (NEU) percentage, red blood cell (RBC) count, hemoglobin (HGB), lymphocyte (LYM) count, and platelet (PLT) count. The rats were anesthetized by an abdominal injection of 2% sodium pentobarbital (1.5 ml/kg). The rats were sacrificed by cervical dislocation after 24 and 72 h. The color and shape of the gross organs were observed. The major organs, including the lungs and liver, were frozen and sectioned for examination. DAPI (4',6-diamidino-2-phenylindole, Sigma-Aldrich) was used for nuclear staining by incubating with the frozen tissue slices at 37 °C for 20 min. Fluorescence imaging of the samples was performed using a Leica TCS SP2 confocal microscope (Leica, Solms, Germany). All of the animal experiments were approved by the Ethics Committee of the General Hospital of Northern Theater Command, China.

2.8. Statistical analysis

Each experiment was performed in triplicate. All of the data are expressed as mean ± SD. The data were analyzed using one-way analysis of variance (ANOVA) followed by Tukey's *post hoc* test. Values of $p < 0.05$ were considered statistically significant.

3. Results

3.1. Synthesis and characterization of nanoparticles

The ACP, Mg-ACP, and Mg-ACP/PAA nanoparticles were synthesized by wet chemical precipitation (Supplementary Fig. S1). After aging at 80 °C for 6 h, ACP and Mg-ACP precursors transformed to HA (JCPDF #09–0432) and Mg-TCP (JCPDF #09–0169) nanocrystals (Fig. 1 A) without diffraction peaks of impurities, whereas Mg-ACP/PAA nanoparticles retained the amorphous state (Fig. 1 A). The FTIR results showed characteristic peaks of PAA molecules at 1701 cm^{-1} (stretching vibration of C=O group) and ~3300 cm^{-1} (broad absorption peak for stretching vibration of OH group; Fig. 1 B), and calcium phosphate at 1020 cm^{-1} and 1067 cm^{-1} (stretching vibration of PO_4^{3-} group) [32,33]. After the chelation of PAA molecules with Ca^{2+} ions, C=O and C–O strongly coupled and obtained the same stretching vibration peaks of COO^- in the FTIR analysis (Fig. 1 B), indicated by peaks of stretching vibration at ~1560 cm^{-1} [34]. These results showed that the PAA molecules preferentially chelated with Ca^{2+} ions to form hybrid materials.

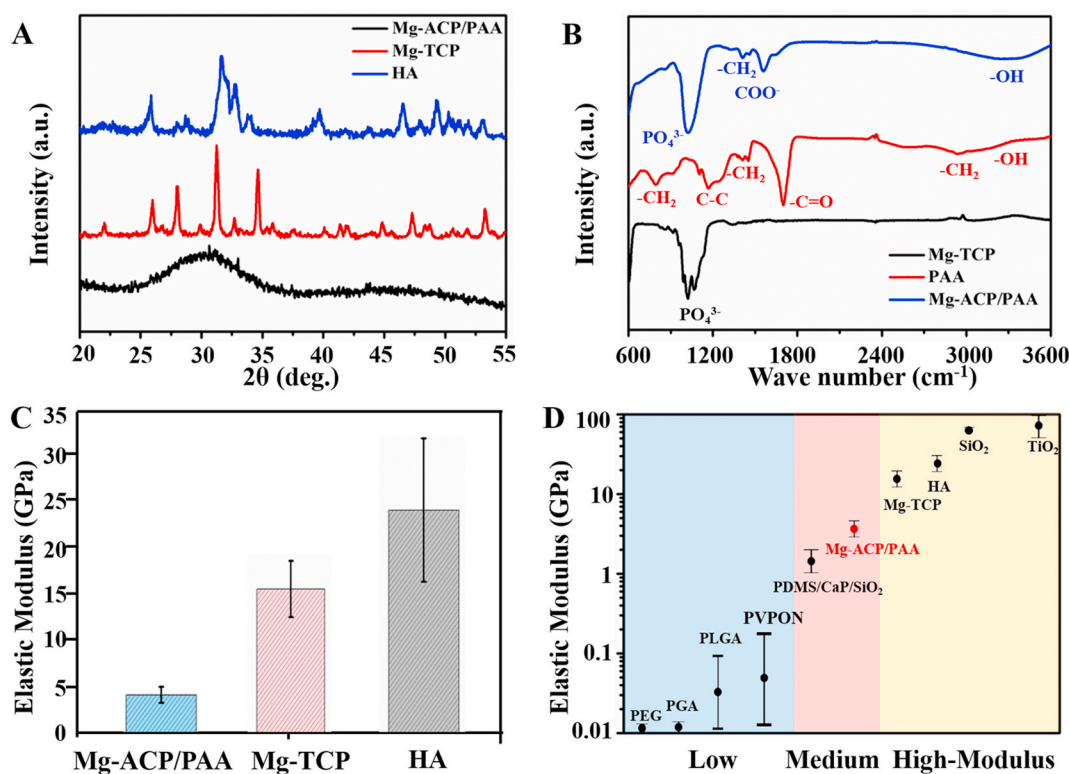The ACP and Mg-ACP powders that were prepared in this study were

Fig. 1. (A) XRD patterns of the synthesized Mg-ACP/PAA, Mg-TCP, and HA nanoparticles. (B) FTIR spectra of Mg-TCP, PAA, and Mg-ACP/PAA samples. (C) Elastic moduli of nanoparticles that were calculated from 100 points in AFM images of Mg-ACP/PAA, Mg-TCP, and HA nanoparticles. (D) Elastic moduli of various nanoparticles from the literature [35–40].

stable for a limited time (~7 days) under ambient conditions (Supplementary Fig. S2 A,B). The chelation of PAA molecules with these Mg-ACP clusters formed inorganic-organic Mg-ACP/PAA hybrid nanoparticles, which were much more stable under ambient conditions (>1 year, Supplementary Fig. S2 C). The TGA/DSC analysis further illustrated thermal stability of the Mg-ACP/PAA nanoparticles following four stages of heat treatment from room temperature to 700 °C (Supplementary Fig. S3 A). Approximately 7.6 wt% surface water relative to total weight was lost in the first stage of heating before 155 °C. In the second stage, 2.4 wt% inside bound water relative to total weight was lost between 155 °C and 315 °C. Therefore, about 10.0 wt% water in total was present in the Mg-ACP/PAA samples. In the third stage (315–400 °C), the decarboxylation of PAA and crystallization from Mg-ACP (~79.3 wt% of total weight) to Mg-TCP occurred. Finally, the combustion reaction of PAA molecules (~10.7 wt% of total weight) occurred between 400 and 700 °C. In addition, EDS analysis showed the presence of Ca, Mg, P, C, O elements in Mg-ACP/PAA nanoparticles (Supplementary Fig. S4). A previous study reveals that ACP consists of pre-nucleation clusters called Posner's clusters with a chemical composition $Ca_9(PO_4)_6$ [14]. The ICP-MS results showed that the molar ratio of Ca/P for Mg-ACP/PAA nanoparticles was about 1.5, consistent well with the Posner's formula (Supplementary Table S1). The Mg content (Mg/(Mg + Ca)) in Mg-ACP was detected as 8.6 ± 0.4 mol% by the ICP-MS analysis (Supplementary Table S1). Therefore, the chemical formula of Mg-ACP can be assumed as $(Ca,Mg)_9(PO_4)_6 \cdot nH_2O$ in the Mg-ACP/PAA samples.

The sizes of the Mg-TCP and HA nanoparticles as prepared were 20.7 ± 3.7 nm and 24.7 ± 4.3 nm, respectively (n = 15; Supplementary Fig. S5 A,C). The interplanar spacing d values for the (2 0 2) and (4 0 2) crystal planes of HA were 2.6 and 1.8 Å, respectively (Supplementary Fig. S5 B), consistent with theoretical d values for the (2 0 2) and (4 0 2) crystal planes of HA (2.631 and 1.754 Å, respectively) based on JCPDF #09–0432. The interplanar spacing d values for the (2 0 20), (0 2 10),

and (1 0 10) crystal planes of Mg-TCP were 1.7, 2.8, and 3.4 Å, respectively (Supplementary Fig. S5 D), consistent with theoretical d values for the (2 0 20), (0 2 10), and (1 0 10) crystal planes of β-TCP (1.728, 2.880, and 3.450 Å, respectively) based on JCPDF #09–0169.

The BET surface area of Mg-ACP/PAA nanoparticles (113.07 ± 0.22 m^2/g) was larger than Mg-TCP (33.54 ± 0.04 m^2/g) and HA (88.09 ± 0.30 m^2/g) nanoparticles because of the hybrid structures of Mg-ACP/PAA nanoparticles (Supplementary Fig. S3 B). The average modulus of the Mg-ACP/PAA, Mg-TCP, and HA samples was calculated based on 100 data points in a selected area of 1 μm × 1 μm using the AFM technique (Supplementary Fig. S6). The average elastic modulus of the Mg-ACP/PAA sample was ~4.3 ± 0.9 GPa, which was significantly lower than the HA (25.2 ± 8.1 GPa) and Mg-TCP (16.8 ± 3.3 GPa) samples (Fig. 1C). Most inorganic nanoparticles, such as SiO_2, TiO_2, and HA, exhibit high stiffness (elastic modulus > 10 GPa), whereas organic nanoparticles, such as PEG, polyglycolic acid (PGA), and poly (lactic-co-glycolic acid) (PLGA), usually exhibit low stiffness (elastic modulus < 0.1 GPa) based on literature (Fig. 1 D) [35–40]. The inorganic-organic hybrid nanoparticles or composites exhibited medium stiffness (0.1 GPa < elastic modulus < 10 GPa; Fig. 1 D).

Transmission electron microscopy bright field imaging at high magnification revealed the Mg-ACP/PAA nanoparticle size of ~24.0 ± 4.8 nm (n = 15; Fig. 2 A), which formed by the assembly of Mg-ACP clusters (~2.1 ± 0.5 nm, n = 15) and PAA molecules (Fig. 2 B). The electron diffraction pattern of the selected area confirmed the amorphous state of Mg-ACP/PAA nanoparticles (Fig. 2C), which was consistent with the XRD results (Supplementary Fig. S1). Fig. 2 D shows the progressive steps of the formation of Mg-ACP/PAA nanoparticles. In the first step, Ca^{2+} ions chelated with PAA molecules when the Ca^{2+}/Mg^{2+} ion solution was slowly added to the phosphate solution. In the second step, PO_4^{3-} ions combined with Ca^{2+} through an electrostatic interaction and formed initial Mg-ACP clusters. In the third step, Mg-ACP clusters and PAA molecules assembled to form inorganic-organic
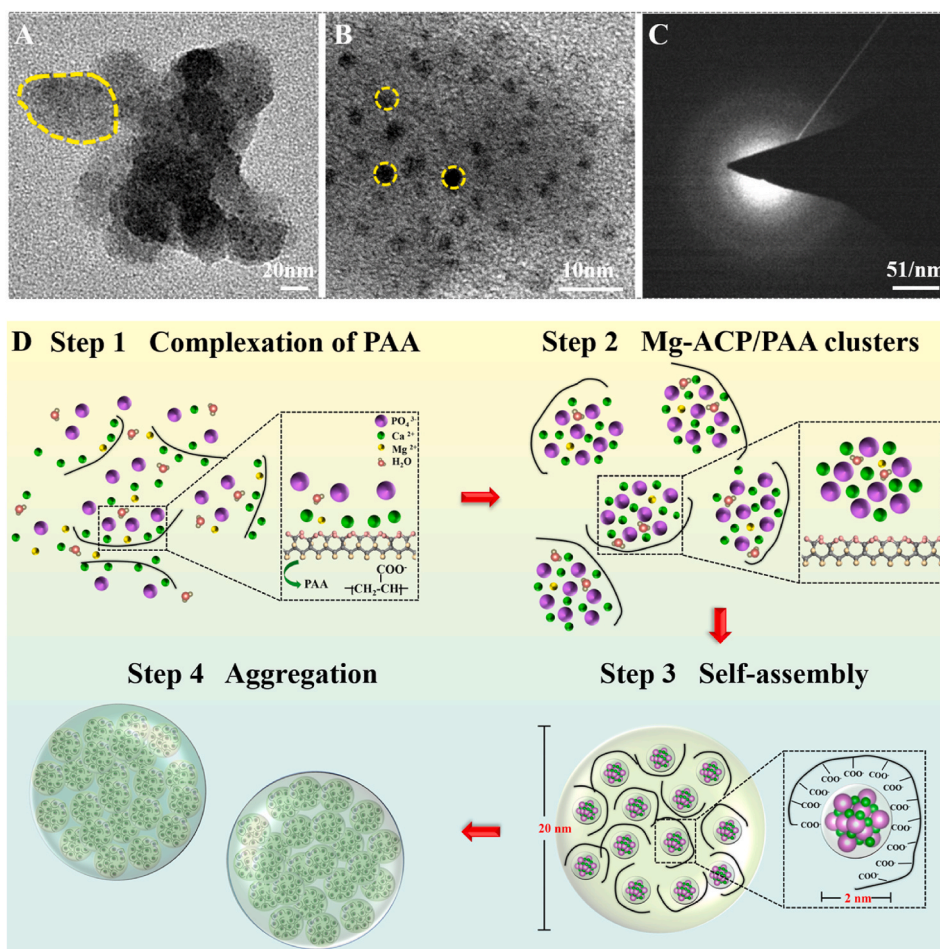
Fig. 2. (A) Transmission electron microscopy bright field image. (B) High-resolution TEM image. (C) Electron diffraction pattern of selected area of Mg-ACP/PAA samples. (D) Schematic diagram of the progressive assembly of Mg-ACP/PAA nanoparticles.

hybrid nanoparticles. Finally, Mg-ACP/PAA aggregates ($\sim$269 $\pm$ 71 nm) formed after the agglomeration progress driven by the decreasing surface energy based on particle size analysis (Supplementary Fig. S7).

3.2. Cellular uptake and cell viability

The cytotoxicity of Mg-ACP/PAA nanoparticles was studied by direct culture with MC3T3-E1 cells. The RTCA was employed to evaluate the interaction between cells and Mg-ACP/PAA nanoparticles. RTCA technology has emerged as an alternative non-invasive and label-free approach to assess cellular proliferation, cytotoxicity, and migration in real time at a cell-culture level [41,42]. The RTCA measures changes in impedance in a meshwork of interdigitated gold microelectrodes that are located at the well bottom (E-plate). Cells were present on top of the adjacent electrodes during the culture, from which impedance could be measured. Larger impedance is associated with a larger number of cells that attach to the electrodes. Thus, the RTCA can provide an index of cell numbers.

In the present study, MC3T3-E1 cells were incubated with different amounts of Mg-ACP/PAA nanoparticles to illustrate their cytotoxicity. The cellular uptake of Mg-ACP/PAA nanoparticles ($\sim$269 nm; Supplementary Fig. S7) was detected in serum-free medium for 4 h to avoid specific effects of serum proteins [43]. The cells were then cultured with normal medium for 36 h. The RTCA curves were calculated between the starting point of nanoparticle treatment and the ending point of cell confluence. The treated and untreated groups exhibited similar trends in the growth of cell proliferation. No dose-dependent response was observed among groups of different nanoparticle concentrations

(17–272 µg/ml; Fig. 3 A,B). The 136 µg/ml Mg-ACP/PAA nanoparticle medium was subsequently used for the following cell culture experiments unless otherwise specified.

The live/dead assay was performed to investigate whether cell membranes were destroyed by the culture with Mg-ACP/PAA nanoparticles. No obvious leakage of Calcein-AM (a cell-membrane-permeant dye that becomes impermeant after hydrolysis by intracellular esterases) from MC3T3-E1 cells after treatment with 136 µg/ml Mg-ACP/PAA nanoparticles for 4 h (Fig. 3 C) compared with the untreated group (Fig. 3 D), suggesting that the cell membranes remained intact during the uptake of these nanoparticles. High MC3T3-E1 cell viability was observed, with very few dead cells, indicated by red PI staining. No significant difference in cell viability was found between the treated group (0.974 $\pm$ 0.012) and untreated group (0.980 $\pm$ 0.003; Supplementary Fig. S8). These results suggest that the internalization of Mg-ACP/PAA nanoparticles into MC3T3-E1 cells did not disturb cell membrane integrity or induce pore formation.

The real-time lens-free microscope images were employed to reveal morphology changes of MC3T3-E1 cells with or without nanoparticle treatment (Supplementary Fig. S9). Area values and aspect ratios for cells were analyzed based on video acquisition for 48 h. After cell seeding for 20 h, the cellular areas (532.957 $\pm$ 279.542 µm^2) and aspect ratios (0.829 $\pm$ 0.142) were obtained before nanoparticle treatment (Fig. 4 A,C). Cellular areas (519.923 $\pm$ 264.050 µm^2) and aspect ratios (0.797 $\pm$ 0.148) were found after nanoparticle treatment for 4 h, close to cellular areas (460.579 $\pm$ 215.358 µm^2) and aspect ratios (0.763 $\pm$ 0.146) after further culture for 24 h in normal culture medium (Fig. 4 A, C). Similar trends for cellular areas and aspect ratios were also found for
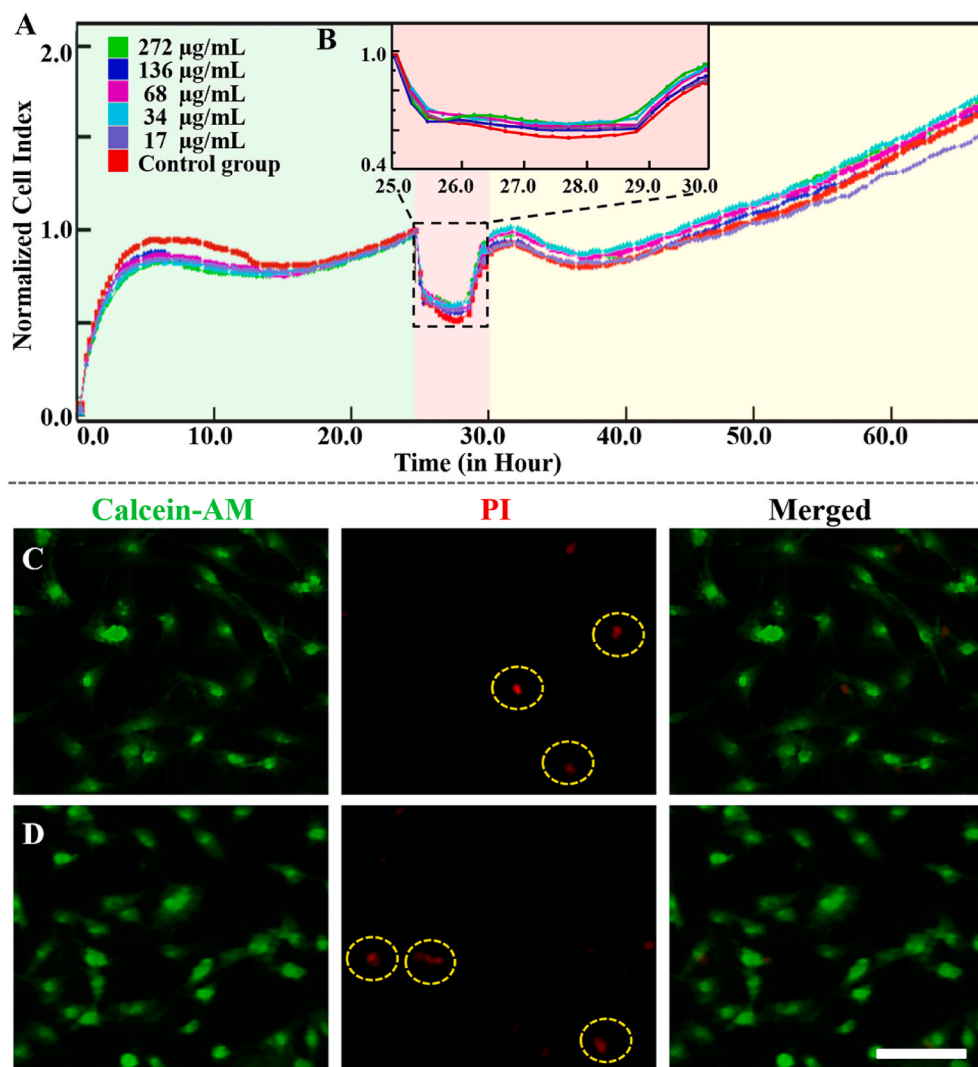
Fig. 3. (A) Normalized cell index for MC3T3-E1 cells that were treated with Mg-ACP/PAA nanoparticles at different concentrations. The cell index was normalized at the time point of treatment (t = 24 h). Cells were cultured with serum-free medium during nanoparticles treatment for 4 h (pink area). (B) Magnified region of interest. (C, D) Confocal laser scanning microscopy images of MC3T3-E1 cells after incubation with (C) or without (D) Mg-ACP/PAA nanoparticles for 4 h, showing Calcein-AM staining (green), PI staining (red), and merged images. Scale bar = 50 μm.

the control group (Fig. 4 B,D). These results suggested that uptake of Mg-ACP/PAA nanoparticles did not affect cell morphology and permeability, which were not cytotoxic at the experimental conditions.

3.3. Cellular uptake and degradation of Mg-ACP/PAA nanoparticles

The internalization of nanoparticles into living cells is crucially important for biomedical applications [44,45]. MC3T3-E1 cells were treated with 136 μg/ml Mg-ACP/PAA/FITC nanoparticles with fluorescence tracking in serum-free α-MEM for 0, 1, and 4 h. The cells were fluorescently stained with FITC after uptake of nanoparticles. The green fluorescence intensity of Mg-ACP/PAA/FITC nanoparticles increased with the increase in incubation time (0, 1, and 4 h; Fig. 5A–C), indicating the continuous uptake of nanoparticles during this period. The high colocalization (yellow color) of Mg-ACP/PAA/FITC nanoparticles (green) and lysosomes (red) was found, confirming the internalization of these nanoparticles through endocytic cycles. Furthermore, degradation of these Mg-ACP/PAA/FITC nanoparticles was observed (Fig. 5 D), with the disappearance of green fluorescence by culture with normal medium for 24 h after uptake of nanoparticles for 4 h.

Cryo-SXT with high spatial resolution (~30 nm) was employed to reveal the three-dimensional distribution of Mg-ACP/PAA nanoparticles and their degradation inside MC3T3-E1cells (Fig. 5 E–H). The Cryo-SXT results showed that Mg-ACP/PAA nanoparticles (~222 ± 81 nm; n = 15) were internalized in MC3T3-E1 cells, and the number of nanoparticles

increased with the increase in incubation time (1, 4 h; Fig. 5 F,G). Only a few Mg-ACP/PAA nanoparticles were detected inside the cells by further culture with normal medium for 24 h after uptake of nanoparticles for 4 h (Fig. 5H), indicating that the majority of nanoparticles were degraded. These results were consistent with the previous fluorescent staining results.

Amorphous calcium phosphate is more labile than crystalline counterparts, such as β-TCP and HA. The Mg^{2+} substitution of Ca^{2+} further increases the solubility of ACP [23,46]. In the present study, Mg-ACP/PAA, Mg-TCP, and HA nanoparticles were dissolved in PBS (pH 5.0 and 5.5) to simulate their degradation in the environment of lysosomes during endocytosis. While dissolving at pH 5.5 for 12 h at a concentration of 1 mg/ml, the dissolved percentage of the Mg-ACP/PAA sample was 28.4%, which was 4.2 times higher than the TCP sample and 8.9 times higher than the HA sample (Fig. 6 A). The solubility of the Mg-ACP/PAA sample (pKs = 13.71) at pH 5.5 was much higher than the HA (pKs = 37.15) and Mg-TCP (pKs = 16.50) samples. Phosphate buffer solutions at pH 5.0 and 6.0 were used to simulate the environment of lysosomes and early endosomes, respectively, during cellular digestion (Fig. 6 B). The majority (~72.4%) of the Mg-ACP/PAA sample (0.2 mg/ml) dissolved in the solution at pH 5.0 in 1 h, which was more stable in the solution at pH 6.0 (~32.8% dissolved). These results suggested that the Mg-ACP/PAA sample was sensitive to pH, which was relatively stable in early endosomes (pH 6.0) and could be efficiently dissolved in lysosomes (pH 5.0) during endocytosis. The efficient degradation of
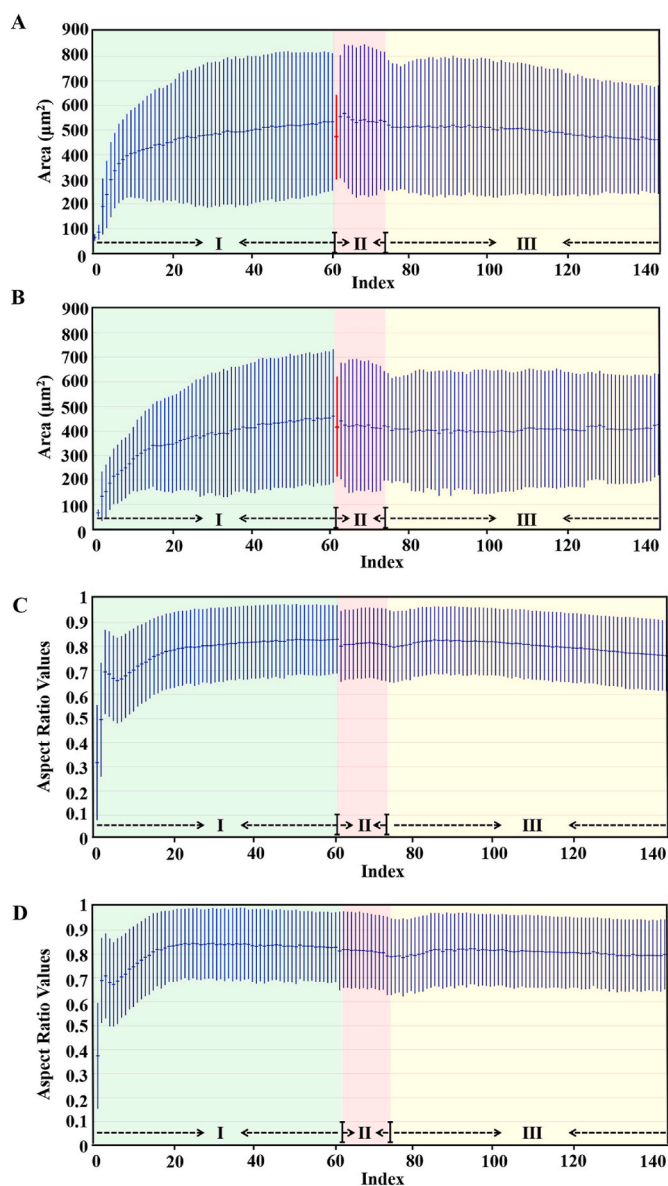
Fig. 4. Analysis of area values (A, B) and aspect ratios (C, D) of MC3T3-E1 cells treated with 136 µg/mL Mg-ACP/PAA nanoparticle medium (A, C) or normal culture medium (B, D, control group) based on video acquisition for 48 h. Blue shadows indicate the stages for initial cell adhesion for 20 h (Phase I). Pink shadows indicate the stages for nanoparticle treatment for 4 h (Phase II). Yellow shadows indicate the continuous culture with normal medium for 24 h (Phase III). The aspect ratios of cells were set between 0 and 1, with 0 being perfectly circular and 1 being elongated.

nanoparticles in lysosomes is likely beneficial to the release of incorporated therapeutic drug molecules or fluorescent imaging molecules [47–49].

The concentrations of intracellular free Ca^{2+} ion levels in MC3T3-E1 cells were evaluated to further reveal the cellular degradation of Mg-ACP/PAA nanoparticles using Fluo-3AM dyes by LSCM and flow cytometry (FACS) analysis (Fig. 6 C). With the increase in the cellular uptake time (0–4 h), the fluorescent intensity slightly increased (7.43 ± 0.75 at 0 h, 8.03 ± 0.26 at 1 h, and 8.54 ± 0.41 at 4 h), indicating an increase in intracellular Ca^{2+} ion concentrations that was likely attributable to the degradation of Mg-ACP/PAA nanoparticles that released Ca^{2+} ions. The Fluo-3 AM fluorescent intensity decreased to 7.95 ± 0.08 when MC3T3-E1 cells cultured with normal medium for 24 h after uptake of nanoparticles, suggesting that the cells adjusted the Ca^{2+} ion

concentration after Mg-ACP/PAA nanoparticle degradation. These results showed that the Mg-ACP/PAA nanoparticles efficiently degraded in lysosomes without cytotoxicity to MC3T3-E1 cells (Fig. 6 C,D), indicating good cytocompatibility.

3.4. Biosafety of Mg-ACP/PAA nanoparticles in vivo

Nanoparticles that cannot degrade sufficiently fast may accumulate in organs and lead to potential toxicity, thus hampering their utility as carriers of therapeutic molecules. To further evaluate the biosafety of the Mg-ACP/PAA nanoparticles and detect and track Mg-ACP/PAA nanoparticles in vivo, Mg-ACP/PAA/FITC nanoparticles that were dispersed in saline solution were injected in the tail vein in rats, and blood biochemistry was assessed 0, 24, and 72 h after the injection. The WBC and NEU values slightly increased 24 h after the intravenous injection of Mg-ACP/PAA/FITC nanoparticles, but these increases were not statistically significant ($p > 0.05$) and returned to the normal range (i.e., the same as the control group) at 72 h (Fig. 7 A). There was no obvious change for RBC, HGB, PLT, and LYM values among different time points (0, 24, and 72 h). These results indicated that a slight inflammatory response occurred after the initial injection of Mg-ACP/PAA nanoparticles, but this inflammatory response normalized over time.

To further evaluate the degradation of Mg-ACP/PAA/FITC nanoparticles in vivo, frozen sections of major organs, including the lungs and liver, were examined. Fig. 7 B-G show LSCM images of frozen lung and liver tissue slices. Weak green fluorescence (yellow arrows) was observed in both the control and experimental groups, but this was considered spontaneous fluorescence in organ tissues and not attributable to the Mg-ACP/PAA/FITC nanoparticles. No obvious aggregation of Mg-ACP/PAA/FITC nanoparticles was observed in the lung and liver tissues, which was likely attributable to the relatively small amount of nanoparticles or rapid degradation in vivo. These in vivo results preliminarily demonstrate that the Mg-ACP/PAA nanoparticles showed good biosafety.

4. Discussion

Amorphous calcium phosphate has been widely found in bone, teeth, and other tissues [12,50] and shown to play an important role in the precursor phase of apatite mineral formation. However, the meta-stability and labile nature of ACP limit further biomedical applications. Mg^{2+} ions are predominantly present at grain boundaries as an intergranular phase of Mg-ACP in both rodent and human enamel, which appears to inhibit transformation of ACP to HA by surface adsorption of Mg^{2+} ions [46,51]. Our results indicated that the ACP and Mg-ACP powders were stable for approximately 7 days under ambient conditions. However, the shelf-life of Mg-ACP powder is not sufficiently long for biomedical applications. Organic molecules, such as PAA and PASP, have been used instead of NCPs to stabilize ACP during biomineralization [9,20]. We prepared inorganic-organic Mg-ACP/PAA hybrid nanoparticles using a biomineralization strategy. The chelation of Ca^{2+} ions in ACP by carboxyl groups in PAA molecules prevented the fusion of Mg-ACP nanoclusters, which could stabilize the Mg-ACP/PAA nanoparticles for longer than 1 year under ambient conditions. Thermal aging treatments of ACP, Mg-ACP and Mg-ACP/PAA nanoparticles at 80 °C were further conducted for evaluation of thermal stability (Fig. 1 A). Our results showed that ACP and Mg-ACP samples crystallized to HA and Mg-TCP, respectively, by thermal aging at 80 °C for 6 h, while Mg-ACP/PAA samples remain amorphous. Moreover, a previous study reported that ACP phase transformed into crystalline phase by thermal aging over 60 °C [52]. These results confirm that Mg-ACP/PAA hybrid materials show improved thermal stability than ACP.

The size of the Mg-ACP clusters in the Mg-ACP/PAA nanoparticles (~24.0 ± 4.8 nm) was approximately 2.1 ± 0.5 nm ($n = 15$). Nudelman et al. reported that stable ACP complexes with a hydrodynamic diameter (D_h) of 30–70 nm formed in the presence of PASP in the reaction solution
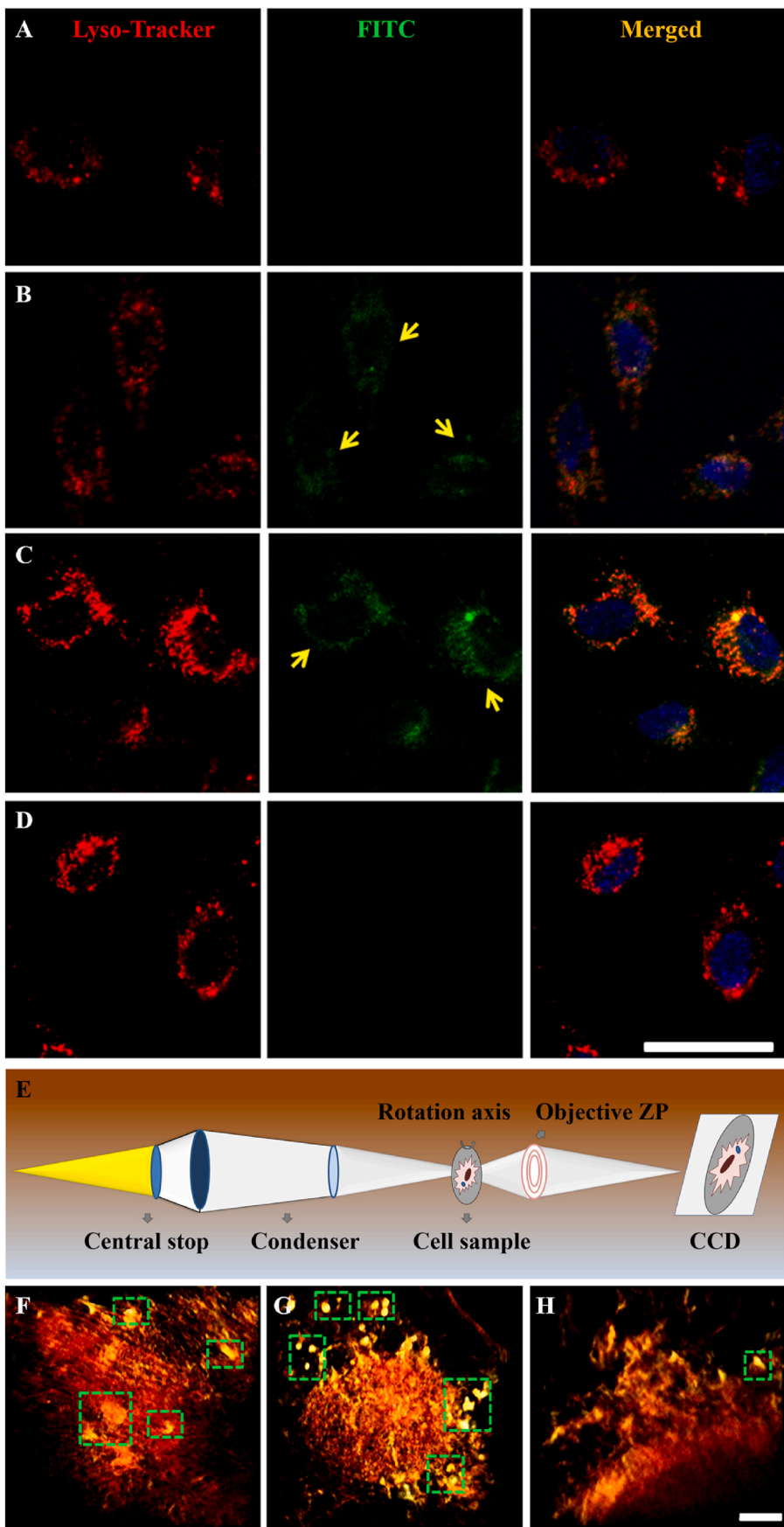
Fig. 5. (A–D) Confocal microscopy image of MC3T3-E1 cells that were incubated with Mg-ACP/PAA/FITC nanoparticles in serum-free medium for 0 h (A), 1 h (B), and 4 h (C), and cells cultured with normal medium for 24 h after uptake of nanoparticles for 4 h (D). Lysosomes were labeled with Lyso-Tracker (red). Nanoparticles were labeled with FITC (green). Cell nuclei were stained with Hoechst (blue). The overlay of green, blue, and red staining shows the colocalization of Mg-ACP/PAA/FITC nanoparticles with lysosomes (yellow) in the merged fluorescence scans. Scale bar = 10 μm. (E) Schematic diagram of the work flow for Cryo-SXT. (F–H) Three-dimensional Cryo-SXT images of MC3T3-E1 cells that were cultured with Mg-ACP/PAA nanoparticles for 1 h (F) and 4 h (G) in serum-free medium and subsequent culture with normal medium for 24 h (H). Scale bar = 2.5 μm.
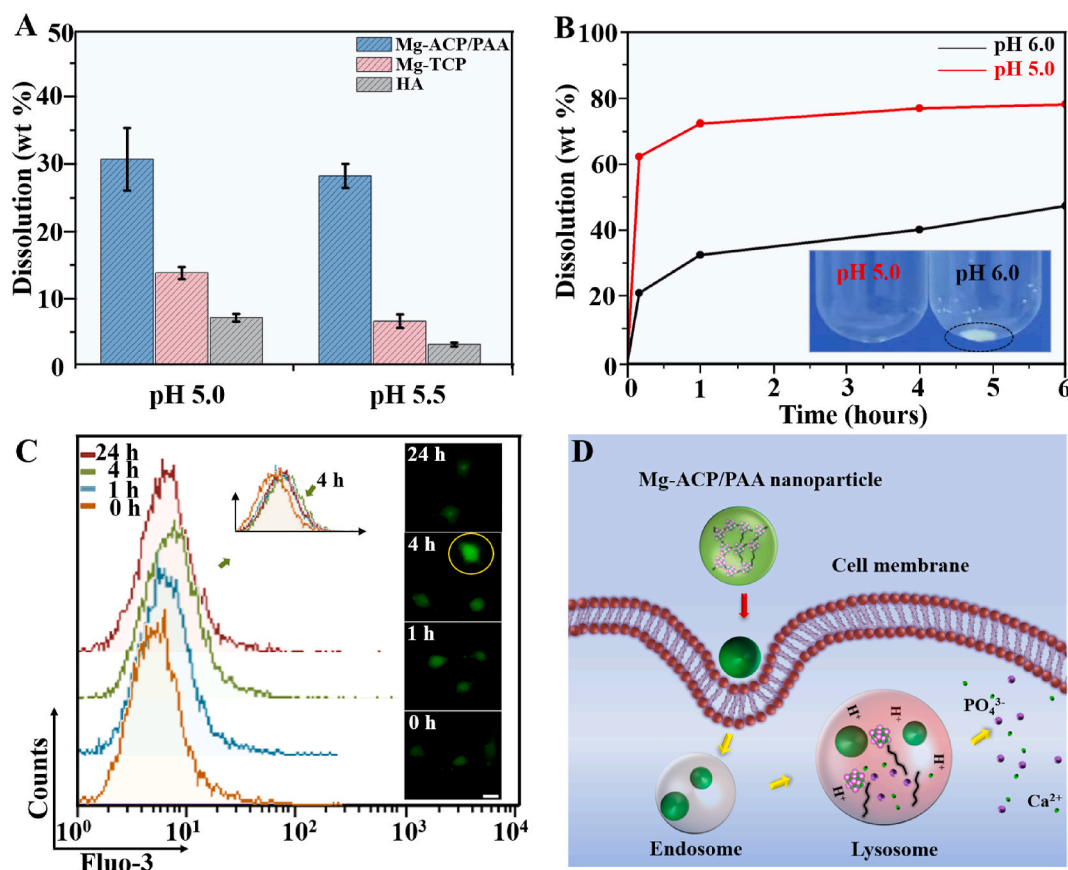
Fig. 6. (A) Dissolution percentages of Mg-ACP/PAA, HA, and TCP nanoparticles in phosphate buffer solution at a concentration of 1 mg/ml and pH 5.0 and 5.5 for 12 h. (B) Dissolution percentages of Mg-ACP/PAA nanoparticles in phosphate buffer solution at a concentration of 0.2 mg/ml and pH 5.0 and 6.0 for 10 min, 1 h, 4 h, and 6 h. (C) FACS analysis of intracellular free Ca^{2+} ion concentrations in MC3T3-E1 cells after uptake of nanoparticles for 0, 1, and 4 h, and in cells cultured with normal medium for 24 h after uptake of nanoparticles (4 h). The inset shows typical fluorescence images of intracellular Ca^{2+} ions in MC3T3-E1 cells with Fluo-3 AM staining (green) in each group. Scale bar = 10 μm. (D) Schematic illustration of the cellular uptake and degradation of Mg-ACP/PAA nanoparticles.

for 10 min, and the size of ACP clusters was approximately 1 nm [9]. The average size of the Mg-ACP clusters was ~2.1 nm in the present study, which was larger than the size that was previously reported (~0.7–1.1 nm) [14], indicating that PAA chelation and Mg substitution synergistically improved the stability of Mg-ACP clusters. These results suggest that ACP clusters of ~2.1 nm can be stabilized by other ions (e.g., Mg^{2+}) and molecules (e.g., PAA or NCPs) during the biomineralization process and serve as the initial seeds that further nucleate and grow to produce apatite minerals.

The internalization pathways for cellular uptake of nanoparticles depend on various factors including the particle size, shape and elasticity [53]. Particle elasticity has been shown to affect cellular uptake and tumor accumulation [54,55]. Nanoparticles with relatively low stiffness, such as nanoliposomes and nanolipogels (<19 MPa), can enter into cells mainly through fusion with the cell membrane, whereas nanoparticles with medium and high stiffness (>0.76 GPa) enter cells by endocytosis [54]. Mg-ACP/PAA hybrid nanoparticles with an elastic modulus of ~4.3 ± 0.9 GPa likely enter cells through endocytosis, based on previous findings [50]. When nanoparticles enter the cell by endocytosis, the endosome lumen becomes slightly acidic (pH 6.0). The fusion of early endosomes with late endosomes ultimately leads to the transport of nanoparticles to lysosomes [56]. Once fused with lysosomes at pH ~5.0, endocytosed nanoparticles can be degraded by acidic pH and digestive enzymes [57,58]. The present fluorescent staining results showed an obvious encapsulation of Mg-ACP/PAA nanoparticles by lysosomes with the further culture of MC3T3-E1 cells for 1 and 4 h after endocytosis, which is consistent with the slight increase in Ca^{2+} levels inside the cells at 4 h MC3T3-E1 cells were further imaged by Cryo-SXT

with a high spatial resolution (~30 nm) to reveal the three-dimensional distribution of Mg-ACP/PAA nanoparticles and their further degradation inside cells. The Cryo-SXT results also showed that Mg-ACP/PAA nanoparticles were internalized in MC3T3-E1 cells, and the number of Mg-ACP/PAA nanoparticles increased as the incubation time increased from 1 to 4 h. A few Mg-ACP/PAA nanoparticles were detected inside the cells after further culture for 24 h, revealed by Cryo-SXT, indicating that the majority of the internalized nanoparticles were degraded.

The inorganic-organic hybrid nanoparticles show advantageous functions for drug delivery compared with traditional inorganic materials, such as silica and hydroxyapatite, in terms of degradation. Recently, hybrid mesoporous organosilica nanoparticles with silsesquioxane framework have been developed, which showed higher degradation efficiency than silica [59,60]. However, the degradation percentage of hybrid organosilica nanoparticles is about 30% when soaked in an acidic solution (pH = 5.0) for 60 h [61]. The degradation percentage of Mg-ACP/PAA nanoparticles was 72.4% when soaked in an acidic solution (pH = 5.0) for 1 h, which showed improved degradation efficiency than hybrid organosilica nanoparticles. Our results suggest that pH-sensitive Mg-ACP/PAA nanoparticles can be efficiently degraded by lysosomes, which are good candidates for the delivery of drugs and other therapeutic molecules [62].

We also evaluated biosafety of the Mg-ACP/PAA nanoparticles. The live/dead assay results showed that lipid membranes of MC3T3-E1 cells remained intact without pore formation after the endocytosis of Mg-ACP/PAA nanoparticles. The RTCA is able to dynamically monitor cell proliferation and toxicity in real time, which also showed that there was no obvious difference for cell proliferation between the groups treated
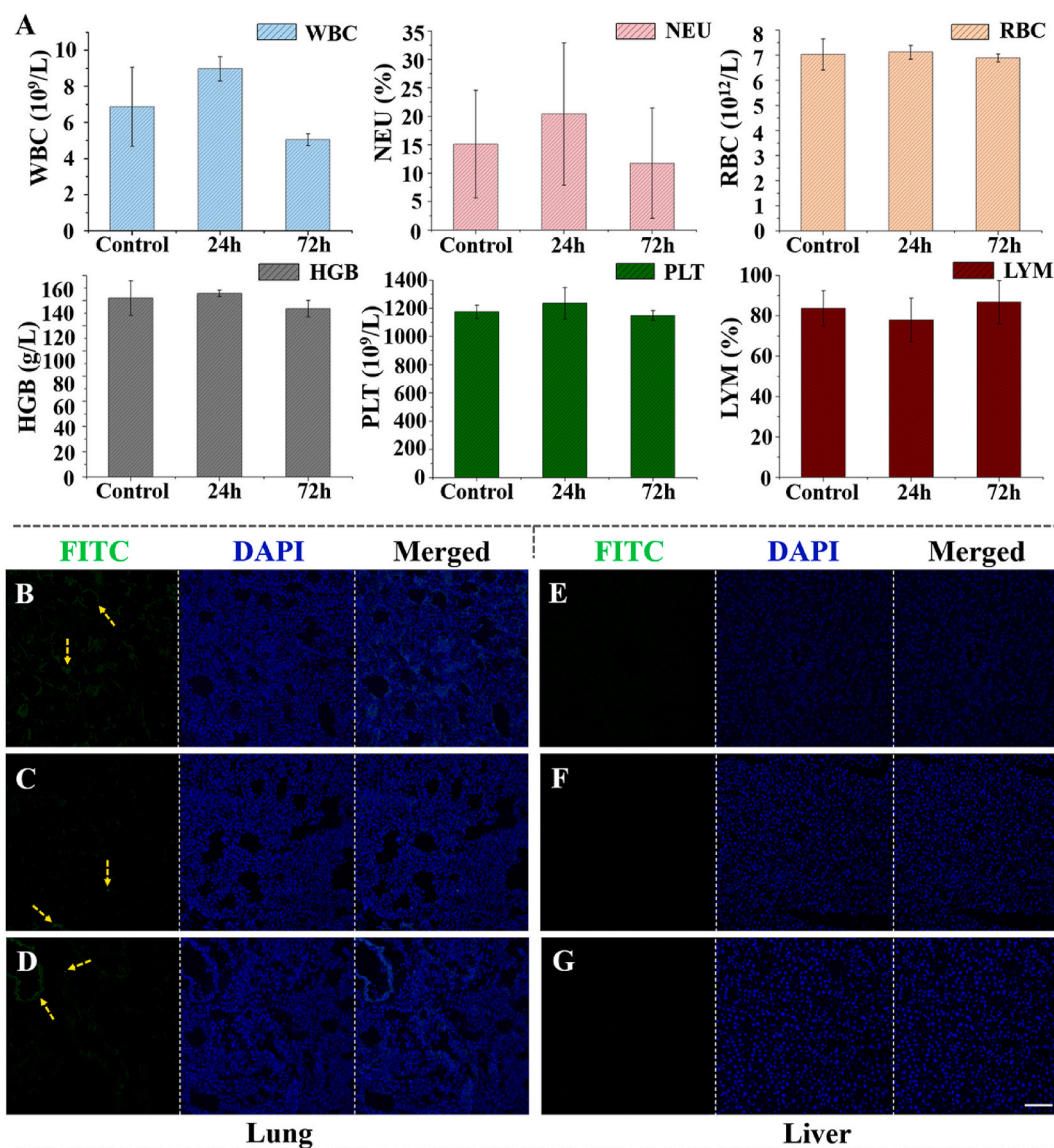
Fig. 7. (A) Results of routine blood analysis, including WBC, NEU, RBC, HGB, PLT, and LYM. (B–G) Laser scanning confocal microscopy images of frozen tissue slices from the lungs (B–D) and liver (E–G). (B, E) Control group. (C, F) Evaluation 24 h after the injection of Mg-ACP/PAA nanoparticles. (D, G) Evaluation 72 h after the injection of Mg-ACP/PAA nanoparticles. Nanoparticles were labeled with FITC (green), and cell nuclei were stained with DAPI (blue). The green and blue panels were merged for B-G. Scale bar = 50 μm in B–H.

with various amounts of nanoparticles and the control group up to 72 h. In addition, the dynamic change of cellular morphology by the lens-free video microscopy suggested that uptake of Mg-ACP/PAA nanoparticles did not affect cell morphology and permeability, which were not cytotoxic at the experimental conditions.

These *in vitro* results showed that no cytotoxicity occurred after the cellular uptake of Mg-ACP/PAA nanoparticles. The *in vivo* results indicated a slight inflammatory response after the initial injection of Mg-ACP/PAA nanoparticles into the tail vein in rats, but this inflammatory response normalized over time (72 h). No aggregation of Mg-ACP/PAA/FITC nanoparticles was found in major organs, such as the lungs and liver, based on the LSCM of tissue slices at 24 and 72 h. These findings suggest that Mg-ACP/PAA nanoparticles have good cytocompatibility and biosafety.

Therefore, these Mg-ACP/PAA hybrid nanoparticles with medium stiffness and efficient degradation in lysosomes may be advantageous for the delivery of therapeutic molecules compared with non-degradable calcium phosphate nanoparticles, which may have good potential for biomedical applications.

5. Conclusions

Inorganic-organic Mg-ACP/PAA hybrid nanoparticles were fabricated using a biomimetic method. The synergistic effects of Mg^{2+} ion substitution and PAA molecule chelation led to good thermal stability of the Mg-ACP/PAA nanoparticles (~20–35 nm) at room temperature. Internalization of the Mg-ACP/PAA nanoparticles into MC3T3-E1 cells was observed through endocytosis, and lipid membranes retained intact without pore formation. We also found that the Mg-ACP/PAA nanoparticles were pH-sensitive and could be efficiently digested in lysosomes under weak acidic conditions. We observed an increase in intracellular Ca^{2+} ion levels during nanoparticle digestion, which reached normal levels after incubation for 24 h, indicating good cytocompatibility. The *in vivo* experiment indicated that the Mg-ACP/PAA nanoparticles were nontoxic. Thus, the present biomineralization strategy was successfully utilized to develop Mg-ACP/PAA hybrid nanoparticles that exhibited efficient cellular degradation and may have good potential for the delivery of therapeutic molecules.

CRediT authorship contribution statement

Na Li: Investigation, Data curation, Writing - original draft. **Wei Cui:** Investigation, Data curation, Writing - original draft. **Peifang Cong:** Investigation, Data curation. **Jie Tang:** Investigation, Writing - original draft. **Yong Guan:** Investigation, Data curation. **Caihao Huang:** Investigation, Data curation. **Yunen Liu:** Data curation, Writing - review & editing. **Chengzhong Yu:** Writing - review & editing. **Rui Yang:** Supervision, Funding acquisition. **Xing Zhang:** Writing - review & editing, Supervision, Funding acquisition.

Declaration of competing interest

The authors declare that they have no known competing financial interests or personal relationships that could have appeared to influence the work reported in this paper.

Acknowledgements

Appendix A. Supplementary data

Supplementary data to this article can be found online at https://doi.org/10.1016/j.bioactmat.2021.01.005.

References

[1] S. Boonrungsiman, E. Gentleman, R. Carzaniga, N.D. Evans, D.W. McComb, A. E. Porter, M.M. Stevens, The role of intracellular calcium phosphate in osteoblast-mediated bone apatite formation, Proc. Natl. Acad. Sci. U.S.A. 109 (2012) 14170–14175.

[2] L. Li, L.Y. Zhang, T.T. Wang, X.T. Wu, H. Ren, C.G. Wang, Z.M. Su, Facile and scalable synthesis of novel spherical Au nanocluster assemblies@polyacryli acid/calcium phosphate nanoparticles for dual-modal imaging-guided cancer chemotherapy, Small 11 (2015) 3162–3173.

[3] J.J. Powell, E. Thomas-McKay, V. Thoree, J. Robertson, R.E. Hewitt, J.N. Skepper, A. Brown, J.C. Hernandez-Garrido, P.A. Midgley, I. Gomez-Morilla, G.W. Grime, K. J. Kirkby, N.A. Mabbott, D.S. Donaldson, I.R. Williams, D. Rios, S.E. Girardin, C. T. Haas, S.F.A. Bruggraber, J.D. Laman, Y. Tanriver, G. Lombardi, R. Lechler, R.P. H. Thompson, L.C. Pele, An endogenous nanomineral chaperones luminal antigen and peptidoglycan to intestinal immune cells, Nat. Nanotechnol. 10 (2015) 361–369.

[4] A.L. Fontaine, A. Zavgorodniy, H. Liu, R. Zheng, M. Swain, J. Cairney, Atomic-scale compositional mapping reveals Mg-rich amorphous calcium phosphate in human dentalenamel, Sci. Adv. 2 (2016), e1601145.

[5] M.B. Sedelnikova, E.G. Komarova, Y.P. Sharkeev, T.V. Tolkacheva, I.A. Khlusov, L. S. Litvinova, K.A. Yurova, V.V. Shupletsova, Comparative investigations of structure and properties of micro-arc wollastonite-calcium phosphate coatings on titanium and zirconium-niobium alloy, Bioact. Mater. 2 (2017) 177–184.

[6] L.V. Sutfin, M.E. Holtrop, R.E. Ogilvie, Microanalysis of individual mitochondrial granules with diameters less than 1000 angstroms, Science 174 (1971) 947–949.

[7] Y. Jiang, Z. Zhou, Y. Zhu, F. Chen, B. Lu, W. Cao, Y. Zhang, Z. Cai, F. Chen, Enzymatic reaction generates biomimic nanominerals with superior bioactivity, Small 14 (2018) 1804321.

[8] T. Iwayama, T. Okada, T. Ueda, K. Tomita, S. Matsumoto, M. Takedachi, S. Wakisaka, T. Noda, T. Ogura, T. Okano, P. Fratz, T. Ogura, S. Murakami, Osteoblastic lysosome plays a central role in mineralization, Sci. Adv. 5 (2019), eaax0672.

[9] F. Nudelman, K. Pieterse, A. George, P.H. Bomans, H. Friedrich, L.J. Brylka, P. A. Hilbers, G. de With, N.A. Sommerdijk, The role of collagen in bone apatite formation in the presence of hydroxyapatite nucleation inhibitors, Nat. Mater. 9 (2010) 1004–1009.

[10] A. Lotsari, A.K. Rajasekharan, M. Halvarsson, M. Andersson, Transformation of amorphous calcium phosphate to bone-like apatite, Nat. Commun. 9 (2018) 4170.

[11] N. Reznikov, M. Bilton, L. Lari, M.M. Stevens, R. Kröger, Fractal-like hierarchical organization of bone begins at the nanoscale, Science 360 (2018), eaao2189.

[12] E. Beniash, R.A. Metzler, R.S.K. Lam, P.U.P.A. Gilbert, Transient amorphous calcium phosphate in forming enamel, J. Struct. Biol. 166 (2009) 133–143.

[13] S. Dorozhkin, Amorphous calcium phosphate, J. Biomater Tiss. Eng. 7 (2010) 27–53.

[14] A. Dey, P.H.H. Bomans, F.A. Müller, J. Will, P.M. Frederik, G. de With, N.A.J. M. Sommerdijk, The role of prenucleation clusters in surface-induced calcium phosphate crystallization, Nat. Mater. 9 (2010) 1010–1014.

[15] J.M. Delgado-López, F. Bertolotti, J. Lyngsø, J.S. Pedersen, A. Cervellino, N. Masciocchi, A. Guagliardi, The synergic role of collagen and citrate in stabilizing amorphous calcium phosphate precursors with platy morphology, Acta Biomater. 49 (2017) 555–562.

[16] M.J. Olszta, X. Cheng, S.S. Jee, R. Kumar, Y.Y. Kim, M.J. Kaufman, E.P. Douglas, L. B. Gower, Bone structure and formation: a new perspective, Math. Sci. Eng. R 58 (2007) 77–116.

[17] M.J. Glimcher, H. Muir, Recent studies of the mineral phase in bone and its possible linkage to the organic matrix by protein-bound phosphate bonds, Philos. Trans. R. Soc. Lond. B Biol. Sci. 304 (1984) 479–508.

[18] Y. Liu, D. Luo, T. Wang, Hierarchical structures of bone and bioinspired bone tissue engineering, Small 12 (2016) 4611–4632.

[19] J.D. Termine, H.K. Kleinman, S.W. Whitson, K.M. Conn, M.L. McGarvey, G. R. Martin, Osteonectin, a bone-specific protein linking mineral to collagen, Cell 26 (1981) 99–105.

[20] S. Yao, X. Lin, Y. Xu, Y. Chen, P. Qiu, C. Shao, B. Jin, Z. Mu, N.A.J.M. Sommerdijk, R. Tang, Osteoporotic bone recovery by a highly bone-inductive calcium phosphate polymer-induced liquid-precursor, Adv. Sci. 6 (2019) 1900683.

[21] C. Shao, B. Jin, Z. Mu, H. Lu, Y. Zhao, Z. Wu, L. Yan, Z. Zhang, Y. Zhou, H. Pan, Z. Liu, R. Tang, Repair of tooth enamel by a biomimetic mineralization frontier ensuring epitaxial growth, Sci. Adv. 5 (2019), eaaw9569.

[22] M. Pavlov, P.E. M Siegbahn, M. Sandstrom, Hydration of beryllium, magnesium, calcium, and zinc ions using density functional theory, J. Phys. Chem. 102 (1998) 219–228.

[23] R. Gelli, M. Scudero, L. Gigli, M. Severi, M. Bonini, F. Ridi, P. Baglioni, Effect of pH and Mg2+ on amorphous magnesium-calcium phosphate (AMCP) stability, J. Colloid Interface Sci. 531 (2018) 681–692.

[24] S.T. Sun, L.B. Mao, Z.Y. Lei, S.H. Yu, H. Colfen, Hydrogels from amorphous calcium carbonate and polyacrylic acid: Bio-inspired materials for "mineral plastics", Angew. Chem. Int. Ed. 55 (2016) 11765–11769.

[25] C.C. Xue, M.H. Li, Y. Zhao, J. Zhou, Y. Hu, K.Y. Cal, Y. Zhao, S.H. Yu, Z. Luo, Tumor microenvironment-activatable Fe-doxorubicin preloaded amorphous CaCO3 nanoformation triggers ferroptosis in target tumor cells, Sci. Adv. 6 (2020), eaax1346.

[26] Y.Y. Liu, J. Jiang, M.R. Gao, B. Yu, L.B. Mao, S.H. Yu, Phase transformation of magnesium amorphous calcium carbonate (Mg-ACC) in a binary solution of ethanol and water, Cryst. Growth Des. 13 (2013) 59–65.

[27] T. Wu, J. Sun, L. Tan, Q. Yan, L. Li, L. Chen, X. Liu, S. Bin, Enhanced osteogenesis and therapy of osteoporosis using simvastatin loaded hybrid system, Bioact. Mater. 5 (2020) 348–357.

[28] T. Wang, Z. Weng, X. Liu, W.K. Yeung, H. Pan, S. Wu, Controlled release and biocompatibility of polymer/titania nanotube array system on titanium implants, Bioact. Mater. 2 (2017) 44–50.

[29] R. Limame, A. Wouters, B. Pauwels, E. Fransen, M. Peeters, F. Lardon, O.D. Wever, P. Pauwels, Comparative analysis of dynamic cell viability, migration and invasion assessments by novel real-time technology and classic endpoint assays, PloS One 7 (2012), e46536.

[30] G. Yan, Q. Du, X. Wei, J. Miozzi, C. Kang, J. Wang, X. Han, J. Pan, H. Xie, J. Chen, W. Zhang, Application of real-time cell electronic analysis system in modern pharmaceutical evaluation and analysis, Molecules 23 (2018) 3280.

[31] J. Liu, F. Li, L. Chen, Y. Guan, L. Tian, Y. Xiong, G. Liu, Y. Tian, Quantitative imaging of Candida utilis and its organelles by soft X-ray Nano-CT, J. Microsc. Oxford 270 (2018) 12650.

[32] Q. Jiang, S. Wang, S. Xu, Preparation and characterization of water-dispersible carbon black grafted with polyacrylic acid by high-energy electron beam irradiation, J. Mater. Sci. 53 (2018) 6106–6115.

[33] W. Cui, Q. Song, H. Su, Z. Yang, R. Yang, N. Li, X. Zhang, Synergistic effects of Mg-substitution and particle size of chicken eggshells on hydrothermal synthesis of biphasic calcium phosphate nanocrystals, J. Mater. Sci. Technol. 36 (2020) 27–36.

[34] I. Rianasari, F. Benyettou, S. Sharma, T. Blanton, S. Kirmizialtin, R. Jagannathan, A chemical template for synthesis of molecular sheets of calcium carbonate, Sci. Rep. 6 (2016) 25393.

[35] A.C. Anselmo, S. Mitragotri, Impact of particles elasticity on particle-based drug delivery systems, Adv. Drug Deliv. Rev. 108 (2017) 51–67.

[36] T. Namazu, Y. Isono, Quasi-static bending test of nano-scale SiO2 wire at intermediate temperatures using AFM-based technique, Sensor Actuat. A-Phys. 104 (2003) 78–85.

[37] M. Yu, L. Xu, F. Tian, Q. Su, N. Zheng, Y. Yang, J. Wang, A. Wang, C. Zhu, S. Guo, X. Zhang, Y. Gan, X. Shi, H. Gao, Rapid transport of deformation-tuned nanoparticles across biological hydrogels and cellular barriers, Nat. Commun. 9 (2018) 2607.

[38] M. Prokopowicz, Atomic force microscopy technique for the surface characterization of sol-gel derived multi-component silica nanocomposites, Colloid. Surface. 504 (2016) 350–357.

[39] S.J. Lee, S.W. Han, S.M. Hyun, H.J. Lee, J.H. Kim, Y.I. Kim, Measurement of Young's modulus and Poisson's ratio for Au films using a visual image tracing system, Curr. Appl. Phys. 9 (2009) 75–78.

[40] M. Humar, D. Arcon, P. Umek, M. Skarabot, I. Musevic, G. Bregar, Mechanical properties of titania-derived nanoribbons, Nanotechnology 17 (2006) 3869–3872.

[41] G. Yan, Z. Zhu, L. Jin, J. Chen, H. Xie, J. Miozzi, F. Lei, X. Wei, J. Pan, Study on the quality evaluation of compound danshen preparations based on the xCELLigence real-time cell-based assay and pharmacodynamic Authentication, Molecules 23 (2018) 2090.

[42] L. Otero-Gonzalez, R. Sierra-Alvarez, S. Boitano, J.A. Field, Application and validation of an impedance-based real time cell analyzer to measure the toxicity of nanoparticles impacting human bronchial epithelial cells, Environ. Sci. Technol. 46 (2012) 10271–10278.

[43] F. Catalano, L. Accomasso, G. Alberto, C. Gallina, S. Raimondo, S. Geuna, C. Giachino, G. Martra, Factors ruling the uptake of silica nanoparticles by mesenchymal stem cells: agglomeration versus dispersions, absence versus presence of serum proteins, Small 11 (2015) 2919–2928.

[44] X. Yi, X. Shi, H. Gao, A universal law for cell uptake of one-dimensional nanomaterials, Nano Lett. 14 (2014) 1049–1055.

[45] I. Roy, A. Bhardwaj, J.C. Joshi, A. Ray, K. Gulati, Fluorophore-doped calcium phosphate nanoparticles for non-toxic biomedical applications, RSC Adv. 4 (2014) 40449–40455.

[46] L.M. Gordon, M.J. Cohen, K.W. MacRenaris, J.D. Pasteris, T. Seda, D. Joester, Amorphous intergranular phases control the properties of rodent tooth enamel, Science 347 (2015) 746–750.

[47] J.O. Onyango, M.S. Chung, C.H. Eng, L.M. Klees, R. Langenbacher, L. Yao, M. An, Noncanonical amino acids to improve the pH response of pHLIP insertion at tumor acidity, Angew. Chem. Int. Ed. 54 (2015) 3658–3663.

[48] L. Ding, X. Zhu, Y. Wang, B. Shi, X. Ling, H. Chen, W. Nan, A. Barrett, Z. Guo, W. Tao, J. Wu, X. Shi, Intracellular fate of nanoparticles with polydopamine surface engineering and a novel strategy for exocytosis-inhibiting, lysosome impairment-based cancer therapy, Nano Lett. 17 (2017) 6790–6801.

[49] T. Ji, D.S. Kohane, Nanoscale systems for local drug delivery, Nano Today 28 (2019) 100765.

[50] A. Akiva, M. Kerschnitzki, I. Pinkas, W. Wagermaier, K. Yaniv, P. Fratzl, L. Addadi, S. Weiner, mineral formation in the larval zebrafish tail bone occurs via an acidic disordered calcium phosphate phase, J. Am. Chem. Soc. 138 (2016) 14481–14487.

[51] H. Ding, H. Pan, X. Xu, R. Tang, Toward a detailed understanding of magnesium ions on hydroxyapatite crystallization inhibition, Cryst. Growth Des. 14 (2014) 763–769.

[52] K. Mohammad, H. Saeed, A. Masoud, K. Asghar, Synthesis of calcium phosphate nanoparticles in deep-eutectic choline chloride-urea medium: investigating the role of synthesis temperature on phase characteristics and physical properties, Ceram. Int. 42 (2016) 2780–2788.

[53] J. Ding, J. Chen, L. Gao, Z. Jiang, Y. Zhang, M. Li, Q. Xiao, S.S. Lee, X. Chen, Engineered nanomedicines with enhanced tumor penetration, Nano Today 29 (2019) 100800.

[54] P. Guo, D. Liu, K. Subramanyam, B. Wang, J. Yang, J. Huang, D.T. Auguste, M.A. Moses, Nanoparticle elasticity directs tumor uptake, Nat. Commun. 9 (2018) 130.

[55] S. Zhang, H. Gao, G. Bao, Physical principles of nanoparticle cellular endocytosis, ACS Nano 9 (2015) 8655–8671.

[56] F.R. McGraw, T.E. McGraw, Endocytic recycling, Nat. Rev. Mol. Cell Biol. 5 (2004) 121–132.

[57] J.P. Luzio, B.M. Mullock, P.R. Pryor, M.R. Lindsay, D.E. James, R.C. Piper, Relationship between endosomes and lysosomes, Biochem. Soc. Trans. 29 (2001) 476–480.

[58] G. Marianna, T. Chiara, S. Giovanni, Nanocarriers for protein delivery to the cytosol: assessing the endosomal escape of poly (Lactide-co-Glycolide)-Poly (ethylene imine) nanoparticles, Nanomaterials 9 (2019) 652.

[59] Y. Chen, Q. Meng, M. Wu, S. Wang, P. Xu, H. Chen, Y. Li, L. Zhang, L. Wang, J. Shi, Hollow mesoporous organosilica nanoparticles: a generic intelligent framework-hybridization approach for biomedicine, J. Am. Chem. Soc. 136 (2014) 16326–16334.

[60] Y. Chen, J. Shi, Chemistry of mesoporous organosilica in nanotechnology: molecularly organic-inorganic hybridization into frameworks, Adv. Mater. 28 (2016) 3235–3272.

[61] L. Yu, Y. Chen, M. Wu, X. Cai, H. Yao, L. Zhang, H. Chen, J. Shi, "Manganese extraction" strategy enables tumor-sensitive biodegradability and theranostics of nanoparticles, J. Am. Chem. Soc. 138 (2016) 9881–9894.

[62] B. Kang, A. Kukreja, D. Song, Y.M. Huh, S. Haam, Strategies for using nanoprobes to perceive and treat cancer activity: a review, J. Biol. Eng. 11 (2017) 13.